

The $s\pm$ pairing symmetry in the pressured $\text{La}_3\text{Ni}_2\text{O}_7$ from electron-phonon coupling

Yucong Yin,¹ Jun Zhan,^{2,3} Boyang Liu,^{1,*} and Xinloong Han^{4,5,†}

¹*Institute of Theoretical Physics, School of Physics and Optoelectronic Engineering, Beijing University of Technology, Beijing, 100124, China*

²*Beijing National Laboratory for Condensed Matter Physics and Institute of Physics, Chinese Academy of Sciences, Beijing 100190, China*

³*School of Physical Sciences, University of Chinese Academy of Sciences, Beijing 100190, China*

⁴*Department of Physics, Capital Normal University, Beijing 100048, China*

⁵*Kavli Institute for Theoretical Sciences, University of Chinese Academy of Sciences, Beijing 100190, China*

(Dated: March 3, 2025)

The recently discovered bilayer Ruddlesden-Popper nickelate $\text{La}_3\text{Ni}_2\text{O}_7$ exhibits superconductivity with a remarkable transition temperature $T_c \approx 80$ K under applied pressures above 14.0 GPa. This discovery of new family of high-temperature superconductors has garnered significant attention in the condensed matter physics community. In this work, we assume the this high-temperature superconductor is mediated by phonons and investigate the pairing symmetry in two distinct models: (i) the full-coupling case, where the $\text{Ni-}d_{x^2-y^2}$ and $\text{Ni-}d_{3z^2-r^2}$ orbitals are treated equally in both interlayer and intralayer coupling interactions, and (ii) the half-coupling case, where the intralayer coupling involves only the $d_{x^2-y^2}$ orbital, while the interlayer coupling is restricted to the $d_{3z^2-r^2}$ orbital. Our calculations reveal that the interlayer coupling favors an $s\pm$ -wave superconducting state, whereas the intralayer coupling promotes an $s++$ -wave symmetry. Additionally, we discuss the implications of pair-hopping interactions on the superconducting properties. These findings provide valuable insights into the pairing mechanisms and symmetry of this newly discovered high-temperature superconductor.

I. INTRODUCTION

The search for a new family of high transition temperature (high- T_c) superconductors remains the central task in the condensed matter community, since the discovery of copper-based high- T_c superconductors¹⁻⁴. Drawing inspiration from the crystal and electronic structures of cuprates, the iron-based superconductors⁵⁻¹⁰ and the recent infinite layer nickelate superconductors¹¹⁻¹⁷ are discovered. Notably, the discovery of superconducting property in bilayer Ruddlesden-Popper nickelate $\text{La}_3\text{Ni}_2\text{O}_7$ (LNO)¹⁸, which exhibits a remarkable transition temperature $T_c \approx 80$ K under high pressure exceeding 14 GPa, has sparked intensive investigation into this novel superconducting material¹⁹⁻⁵⁴. Subsequent studies¹⁹⁻²¹ have further confirmed the observation of zero electrical resistance, solidifying LNO as a promising candidate for further exploration in the field of high- T_c superconductivity. Increasing pressure causes the structure to undergo a transition from the orthorhombic structure of the Amam space group to a regular AA-stacking structure of the Fmmm space group. In contrast to the d^9 electronic configuration in cuprates, the normal valence band in LNO manifests the $d^{7.5}$ configuration^{18,20}. The density functional theory (DFT) further reveals that the band structure in the vicinity of the Fermi level under pressure is mainly dominated by the $\text{Ni-}d_{x^2-y^2}$ and $\text{Ni-}d_{3z^2-r^2}$ orbitals¹⁸. These different features imply the fundamental diverse pairing symmetry from the cuprates. Interestingly, in addition to superconductivity, the charge/spin density wave, and non-Fermi-liquid behavior are also suggested by transport measurements^{18,20,52,53}.

A fundamental question in the study of this new fam-

ily of high- T_c superconductors revolves around elucidating the underlying superconducting mechanism. Current theoretical efforts have predominantly focused on understanding superconductivity in terms of the unique band structure and electronic correlations present in this material. However, recent experimental findings suggest that electron-phonon coupling may play a pivotal role in determining the electronic properties. The ongoing debate among several research groups on the strength of electron-phonon coupling⁵⁵⁻⁵⁹ raises a critical question: What would be the pairing symmetry in pressurized LNO if the superconducting state is indeed mediated by electron-phonon (e -ph) coupling?

To address this question, we present a systematic investigation of the superconducting pairing symmetry within the framework of BCS theory by solving the linearized gap equations in momentum space. Specifically, we introduce and analyze two distinct models: (i) the full-coupling case, where the $\text{Ni-}d_{x^2-y^2}$ and $\text{Ni-}d_{3z^2-r^2}$ orbitals are treated on an equal footing in the interactions, and (ii) the half-coupling case, where the intralayer coupling involves only the $d_{x^2-y^2}$ orbital, while the interlayer coupling is restricted to the $d_{3z^2-r^2}$ orbital. Our calculations reveal that the interlayer coupling favors a spin-singlet $s\pm$ pairing symmetry, whereas the intralayer coupling competes by stabilizing a spin-singlet $s++$ pairing symmetry.

The remainder of this paper is organized as follows. In the section II, we introduce our two BCS models band model and demonstrate the method to investigate the superconducting pairing symmetry. In the section III and IV, we present the numerical results in the full-coupling case and in the half-coupling case, respectively. In sec-

tion V, we further discuss the role of pair hopping term in determining the pairing symmetry. Finally, in the section VI we give our further discussions and conclude this paper.

II. MODEL AND METHOD

The low-energy electronic structure of bilayer $\text{La}_3\text{Ni}_2\text{O}_7$, as revealed by DFT calculations and experiments, is predominantly governed by the Ni- $d_{x^2-y^2}$ and $d_{3z^2-r^2}$ orbitals^{18,22–24}. Motivated by this orbital-selective character, we take a minimal bilayer two-orbital model adapted from Ref.²². This effective model successfully encapsulates the essential features of the low-energy band structure near the Fermi level, including orbital hybridization effects and interlayer coupling mechanisms. The model reads

$$H_0 = \sum_{\mathbf{k}\sigma} \Psi_{\mathbf{k}\sigma}^\dagger [H_0(\mathbf{k}) - \mu] \Psi_{\mathbf{k}\sigma}, \quad (1)$$

where the basis is defined as $\Psi_\sigma = (c_{tx^2\sigma}, c_{tz^2\sigma}, c_{bx^2\sigma}, c_{bz^2\sigma})^T$ with field operator $c_{\eta\alpha\sigma}$ denotes the annihilation of an electron with spin $\sigma = \uparrow, \downarrow$ in the top ($\eta = t$) or bottom ($\eta = b$) layer. The orbital index x^2 (z^2) labels the Ni- $d_{x^2-y^2}$ ($d_{3z^2-r^2}$) orbital. The chemical potential is denoted by μ . The matrix H_0 is written as

$$H_0(\mathbf{k}) = \begin{pmatrix} T_{\mathbf{k}}^{x^2} & V_{\mathbf{k}} & t_{\perp}^{x^2} & V'_{\mathbf{k}} \\ V_{\mathbf{k}} & T_{\mathbf{k}}^{z^2} & V'_{\mathbf{k}} & t_{\perp}^{z^2} \\ t_{\perp}^{x^2} & V'_{\mathbf{k}} & T_{\mathbf{k}}^{x^2} & V_{\mathbf{k}} \\ V'_{\mathbf{k}} & t_{\perp}^{z^2} & V_{\mathbf{k}} & T_{\mathbf{k}}^{z^2} \end{pmatrix} \quad (2)$$

with

$$T_{\mathbf{k}}^\eta = 2t_1^\eta(\cos k_x + \cos k_y) + 4t_2^\eta \cos k_x \cos k_y + \epsilon^\eta, \quad (3)$$

$$V_{\mathbf{k}} = 2t_3(\cos k_x - \cos k_y), V'_{\mathbf{k}} = 2t_4(\cos k_x - \cos k_y). \quad (4)$$

Here $T^{\eta=x^2, z^2}$ represents the intralayer intraorbital hopping term, while $V_{\mathbf{k}}$ ($V'_{\mathbf{k}}$) demonstrates the interorbital intralayer (interlayer) hopping. $t_{\perp}^{x^2}$ ($t_{\perp}^{z^2}$) denotes the interlayer hopping term in Ni- $d_{x^2-y^2}$ ($d_{3z^2-r^2}$) orbital. The detailed values of hopping parameters t_1^η , t_2^η , t_3 , t_4 can be found in the reference²². Fig. 1(a) presents the calculated band structures of the system, while panels (b)-(d) display the corresponding Fermi surfaces at three representative chemical potentials. In addition to the prominent high- T_c superconducting regime near the critical doping level reported in Ref.¹⁸, we systematically investigate two characteristic doping scenarios: (i) a hole-doped regime with $\mu = -0.328\text{eV}$, where the Fermi surface topology exhibits a van Hove singularity, and (ii) an electron-doped regime with $\mu = 0.1\text{eV}$. Fig. 1(b-d) reveals that there exist three Fermi surfaces: two hole-like pockets β and γ originating from the interlayer antibonding states of the Ni- $d_{x^2-y^2}$ and bonding state of $d_{3z^2-r^2}$

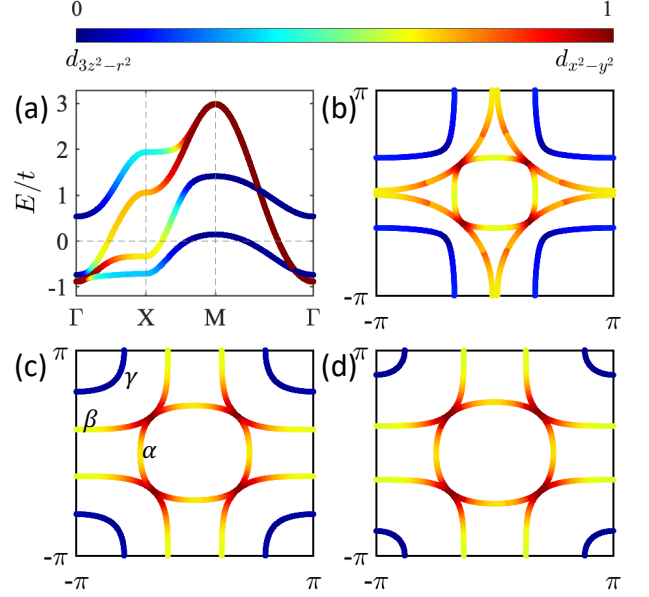


FIG. 1. The orbital-weight band structure²² (a) and Fermi surfaces (b-d) of the bilayer tight-binding model in the pressured LNO. (b) labels the Fermi surface with $\mu = -0.328\text{eV}$ where it manifest a van Hove singularity. (c) and (d) illustrates the Fermi surface with $\mu = 0\text{eV}$ and 0.1eV , respectively.

orbitals; one electron-like pocket formed by the interlayer bonding states of both $d_{x^2-y^2}$ and $d_{3z^2-r^2}$ orbitals. Notably, the orbital-projection analysis demonstrates that the γ pocket predominantly derives its spectral weight from the $d_{3z^2-r^2}$ orbital character.

To elucidate the superconductivity mediated by e -ph coupling in the pressured LNO, we implement two distinct Bardeen-Cooper-Schrieffer (BCS) effective pairing interactions. The first one is the full-coupling case which reads

$$H_I^f = -g_1^f \sum_{\eta\alpha s s'; \mathbf{k}, \mathbf{k}'} \left[c_{\eta\alpha s}^\dagger(\mathbf{k}) c_{\eta\alpha s'}^\dagger(-\mathbf{k}) c_{\eta\alpha s'}(-\mathbf{k}') c_{\eta\alpha s}(\mathbf{k}') \right] - g_2^f \sum_{\alpha s s'; \mathbf{k}, \mathbf{k}'} \left[c_{t\alpha s}^\dagger(\mathbf{k}) c_{b\alpha s'}^\dagger(-\mathbf{k}) c_{b\alpha s'}(-\mathbf{k}') c_{t\alpha s}(\mathbf{k}') \right], \quad (5)$$

in which we take two orbital on equal footing when considering the intralayer or interlayer interactions. The parameters g_1^f and g_2^f represents the intralayer and interlayer pairing strength within the same orbital, respectively, for the full-coupling case. The second type of interacting Hamiltonian is written as

$$H_I^h = -g_1^h \sum_{\eta s s'; \mathbf{k}, \mathbf{k}'} \left[c_{\eta x^2 s}^\dagger(\mathbf{k}) c_{\eta x^2 s'}^\dagger(-\mathbf{k}) c_{\eta x^2 s'}(-\mathbf{k}') c_{\eta x^2 s}(\mathbf{k}') \right] - g_2^h \sum_{s s'; \mathbf{k}, \mathbf{k}'} \left[c_{tz^2 s}^\dagger(\mathbf{k}) c_{bz^2 s'}^\dagger(-\mathbf{k}) c_{bz^2 s'}(-\mathbf{k}') c_{tz^2 s}(\mathbf{k}') \right], \quad (6)$$

which is referred to as the half-coupling case, where we

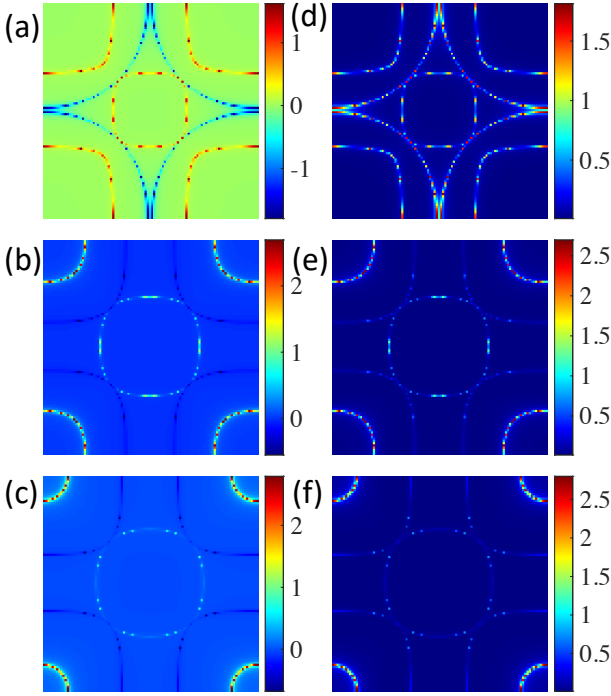


FIG. 2. The pairing gap in the full-coupling case with different parameters. (a), (b) and (c) illustrates the numerical result with only interlayer coupling $g_2^f = 0.12$ for $\mu = -0.328eV$, $0eV$ and $0.1eV$ respectively. (d), (e) and (f) illustrates the numerical result with only intralayer coupling $g_1^f = 0.06$ for $\mu = -0.328eV$, $0eV$ and $0.1eV$ respectively.

only consider the intralayer BCS pairing interaction occurring in the $d_{x^2-y^2}$ orbital, while the interlayer BCS pairing interaction occurs in the $d_{3z^2-r^2}$ orbital. The parameter g_1^h (g_2^h) is the intralayer (interlayer) interaction strength. The intralayer interaction in this model is attributed to the coupling of the B_{1g} phonon mode, which involves the in-plane motion of oxygen atoms, to the $d_{x^2-y^2}$ orbital. In contrast, the interlayer interaction is associated with two A_{1g} phonon modes, which are strongly coupled to the $d_{3z^2-r^2}$ orbital. The the low-energy Hamiltonian H is $H = H_0 + H_I^{f,h}$. The orbital and layer basis $c_{\eta\alpha s}(\mathbf{k})$ can be mapped to the band basis $c_{bs}(\mathbf{k})$ by introducing a unitary matrix as

$$c_{\eta\alpha s}(\mathbf{k}) = \sum_{\beta} U_{\eta\alpha\beta}(\mathbf{k}) c_{\beta s}(\mathbf{k}) \quad (7)$$

where β is the band index. Here we only consider the intraband pairing, thus the projected interacting Hamiltonian is

$$H_{BCS} = - \sum_{\mathbf{k}, \mathbf{k}'} \sum_{bb'; ss'} g^{\beta, \beta'}(\mathbf{k}, \mathbf{k}') c_{\beta s}^{\dagger}(\mathbf{k}) c_{\beta' s'}^{\dagger}(-\mathbf{k}) \times c_{\beta' s'}(-\mathbf{k}') c_{\beta s}(\mathbf{k}') \quad (8)$$

and we define $g^{\beta, \beta'}(\mathbf{k}, \mathbf{k}') = g_1^{\beta, \beta'}(\mathbf{k}, \mathbf{k}') + g_2^{\beta, \beta'}(\mathbf{k}, \mathbf{k}')$ where $g_1^{\beta, \beta'}$ and $g_2^{\beta, \beta'}$ comes from the contribution of the

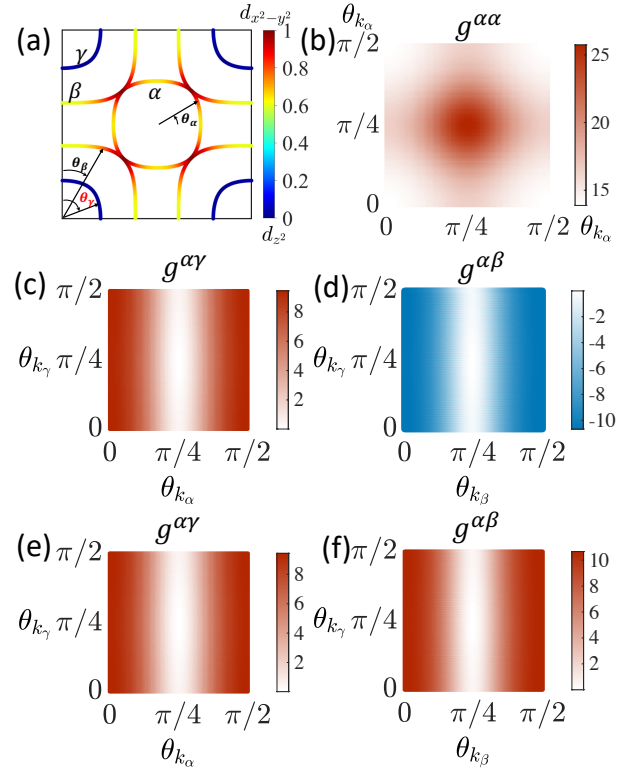


FIG. 3. (a) The momentum distribution at Fermi surfaces when calculating effective interacting strength with fixed $\mu = 0eV$. Effective interacting strength $g^{\alpha\alpha}$ (b), $g^{\alpha\gamma}$ (c) and $g^{\alpha\beta}$ (d) obtained in the full-coupling case with the pure interlayer coupling $g_2^f = 0.12$. Effective interacting strength $g^{\alpha\gamma}$ (e) and $g^{\alpha\beta}$ (f) obtained in the full-coupling case with the pure intralayer coupling $g_1^f = 0.06$.

intralayer and interlayer, respectively. Within the mean-field approximation, we introduce the order parameters $\Delta_{ss'}^{(\beta)}(\mathbf{k})$ by the following

$$\Delta_{ss'}^{(\beta)}(\mathbf{k}) \equiv \sum_{\beta'} \sum_{\mathbf{k}'} g^{\beta, \beta'}(\mathbf{k}, \mathbf{k}') \langle c_{\beta' s'}(-\mathbf{k}') c_{\beta s}(\mathbf{k}') \rangle. \quad (9)$$

To get the gap equation, we introduce the Bogoliubov quasiparticles $a_{\beta}(\mathbf{k})$ and $a_{\beta}^{\dagger}(-\mathbf{k})$ and they can be connected to original creation and annihilation operators $c_{\beta}(\mathbf{k})$ by the following Bogoliubov transformation

$$c_{\beta\uparrow}(\mathbf{k}) = u_{\beta\mathbf{k}} a_{\beta}(\mathbf{k}) + v_{\beta\mathbf{k}} a_{\beta}^{\dagger}(-\mathbf{k}), \quad (10)$$

$$c_{\beta\downarrow}^{\dagger}(-\mathbf{k}) = -v_{\beta\mathbf{k}} a_{\beta}(-\mathbf{k}) + u_{\beta\mathbf{k}} a_{\beta}^{\dagger}(\mathbf{k}), \quad (11)$$

with parameters

$$u_{\beta\mathbf{k}}^2 = \frac{1}{2} \left(1 + \frac{\varepsilon_{\beta}(\mathbf{k})}{E_{\beta}(\mathbf{k})} \right), v_{\beta\mathbf{k}}^2 = \frac{1}{2} \left(1 - \frac{\varepsilon_{\beta}(\mathbf{k})}{E_{\beta}(\mathbf{k})} \right), \quad (12)$$

where $\varepsilon_{\beta}(\mathbf{k})$ denotes β -band's energy and $E_{\beta}(\mathbf{k}) = \sqrt{\varepsilon_{\beta}^2(\mathbf{k}) + |\Delta_{ss'}^{(\beta)}(\mathbf{k})|^2}$ is the energy of Bogoliubov quasiparticle. Putting Eq. (10-12) into Eq. 9, one can derive

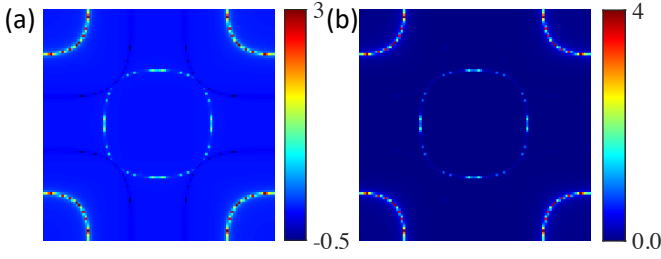


FIG. 4. The pairing gap with fixed interlayer coupling $g_2^f = 0.12$ while varying intralayer coupling $g_1^f = 0.01$ (a) and 0.07 (b) in the full-coupling case with chemical potential $\mu = 0$.

the linear gap equations which read

$$\chi_{\mathbf{k},\mathbf{k}'}^{(\beta,\beta')} = g^{\beta,\beta'}(\mathbf{k},\mathbf{k}') \frac{\tanh\left[\frac{\varepsilon_{\beta'}(\mathbf{k}')}{2k_B T}\right]}{2\varepsilon_{\beta'}(\mathbf{k}')}, \quad (13)$$

near the superconducting transition temperature T_c . The superconducting transition temperature T_c is the highest temperature such that the matrix $\chi_{\mathbf{k},\mathbf{k}'}^{(\beta,\beta')}$ yields eigenvalue 1 in the discrete momentum and band spanned space⁶⁰.

III. SUPERCONDUCTING STATE FOR THE FULL-COUPLING CASE

We begin by systematically analyzing the full-coupling case defined in Eq. 5. In the band space, the interacting strength $g_1^{\beta,\beta'}(\mathbf{k},\mathbf{k}')$ from the contribution of intralayer coupling is

$$g_1^{\beta,\beta'}(\mathbf{k},\mathbf{k}') = g_1^f \sum_{\eta\alpha} U_{\eta\alpha\beta}^*(\mathbf{k}) U_{\eta\alpha\beta}^*(-\mathbf{k}) U_{\eta\alpha\beta'}(-\mathbf{k}') \times U_{\eta\alpha\beta'}(\mathbf{k}'), \quad (14)$$

and $g_2^{\beta,\beta'}(\mathbf{k},\mathbf{k}')$ contributed by the interlayer coupling is

$$g_2^{\beta,\beta'}(\mathbf{k},\mathbf{k}') = g_2^f \sum_{\alpha} U_{t\alpha\beta}^*(\mathbf{k}) U_{b\alpha\beta}^*(-\mathbf{k}) U_{b\alpha\beta'}(-\mathbf{k}') \times U_{t\alpha\beta'}(\mathbf{k}'). \quad (15)$$

After putting $g^{\beta,\beta'}(\mathbf{k},\mathbf{k}') = g_1^{\beta,\beta'}(\mathbf{k},\mathbf{k}') + g_2^{\beta,\beta'}(\mathbf{k},\mathbf{k}')$ into Eq. (13), we can numerically obtain the pairing gap by solving Eq. (9) and (13).

To clearly understand the role of intralayer and interlayer coupling in the pairing symmetry, we separately examine the intralayer and interlayer couplings and plot the resulting pairing symmetries for various doping levels in Fig. 2. Fig. 2(a-c) show that the pairing symmetry induced by the interlayer BCS coupling in the full-coupling case results in pairing gaps with the same sign in the α and γ pockets, while the gap between the α and β pockets has the opposite sign, for fixed parameters $g_1^f = 0$ and $g_2^f = 0.12$ under various doping conditions. Thus, our numerical calculations for the full-coupling case with only

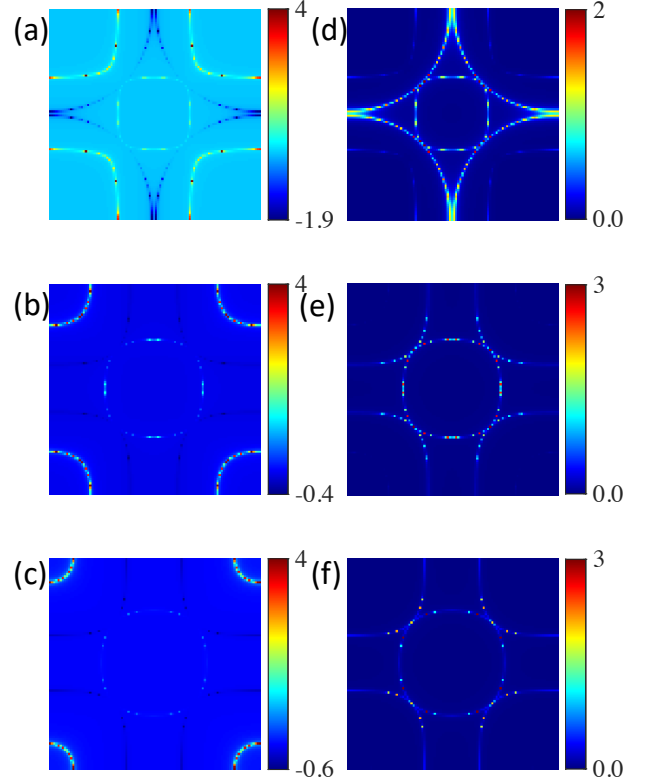


FIG. 5. The pairing gap in the half-coupling case with different parameters. (a), (b) and (c) illustrates the numerical result with only interlayer coupling $g_2^f = 0.18$ for $\mu = -0.328eV, 0eV$ and $0.1eV$ respectively. (d) The result with parameters $g_1^f = 0.11, g_2^f = 0$ and $\mu = -0.328eV$. (e) The result with parameters $g_1^f = 0.17, g_2^f = 0$ and $\mu = 0eV$. (f) The result with parameters $g_1^f = 0.195, g_2^f = 0$ and $\mu = 0.1eV$.

the interlayer coupling indicate that the superconducting state hosts an $s\pm$ -wave pairing symmetry. Furthermore, to address the origin of the $s\pm$ pairing symmetry induced by interlayer coupling, we plot the pairing interactions in the band space in Fig. 3(a-c). As illustrate in Fig. 3(a,b), the pairing interaction $g^{\alpha,\alpha}$ and $g^{\alpha,\gamma}$ indicate negative Josephson coupling both within α intra-Fermi pocket and between α and γ Fermi pockets, intriguing to pairing gaps with the same sign within the same Fermi pockets and between α and γ Fermi pockets. Meanwhile, the negative $g^{\alpha,\beta}$ will favor the opposite sign pairing gap between α and β Fermi pockets. Conversely, the pure intralayer coupling scenario will sustains the conventional $s++$ -wave superconducting state with uniform pairing gap across all pockets as shown in Fig. 2(d-e) with fixed parameter $g_1^f = 0.06$ and $g_2^f = 0$.

The competition between these two pairing channels manifests a superconducting phase transition in the (g_1^f, g_2^f) parameter space. Fig. 4 explicitly demonstrates that increasing the intralayer coupling strength g_1^f drives a phase transition from the $s\pm$ -wave to $s++$ -wave super-

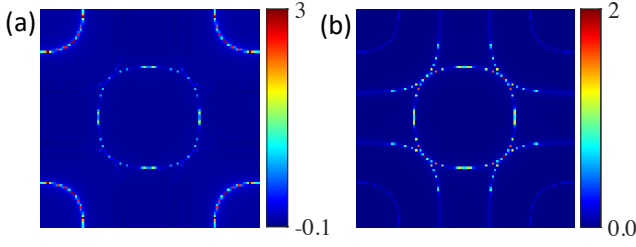


FIG. 6. The pairing gap in the half-coupling case with fixed interlayer coupling $g_2^h = 0.18$ while varying intralayer coupling $g_1^h = 0.165$ (a) and 0.18 (b) with chemical potential $\mu = 0$

conducting ground state, marked by the suppression of inter-pocket gap sign reversal.

IV. PAIRING SYMMETRY IN HALF-COUPLING CASE

In this section, we further investigate the superconducting pairing symmetry in half-coupling case which is demonstrated in Eq. 6. In this case the interaction strength $g^{\beta,\beta'}$ is followed by

$$g_1^{\beta,\beta'}(\mathbf{k}, \mathbf{k}') = g_1^h \sum_{\eta} U_{\eta x^2 \beta}^*(\mathbf{k}) U_{\eta x^2 \beta}^*(-\mathbf{k}) U_{\eta x^2 \beta'}(-\mathbf{k}') \times U_{\eta x^2 \beta'}(\mathbf{k}'), \quad (16)$$

and $g_2^{\beta,\beta'}(\mathbf{k}, \mathbf{k}')$ contributed by the interlayer coupling is

$$g_2^{\beta,\beta'}(\mathbf{k}, \mathbf{k}') = g_2^h U_{tz^2 \beta}^*(\mathbf{k}) U_{bz^2 \beta}^*(-\mathbf{k}) U_{bz^2 \beta'}(-\mathbf{k}') U_{t\alpha \beta'}(\mathbf{k}'). \quad (17)$$

where $g_{1,2}^h$ is the intralayer or interlayer pairing strength in the half coupling case as mentioned before.

Following the methodology employed in the full-coupling scenario, we systematically investigate the individual effects of intralayer and interlayer couplings. By numerically solving the self-consistent equations Eq. (9) and (13) with the interaction $g^{\beta,\beta'}$, we plot the pairing gaps in Fig. 5. As shown in Fig. 5(a-c) with fixed parameters $g_1^h = 0$ and $g_2^h = 0.18$ with several doping conditions, the interlayer coupling also favors the s_{\pm} -wave pairing symmetry as the same as in the full-coupling case. In Fig. 5(d-e), we use the different intralayer coupling strengths g_1^h to drive the superconducting state and obtain the pairing gap under different doping conditions. Then we reach the same conclusion in the half-coupling case as in the full-coupling scenario, the intralayer coupling g_1^h also tends to induce the conventional s_{++} -wave pairing symmetry, due to the same reasons as discussed in the full-coupling case.

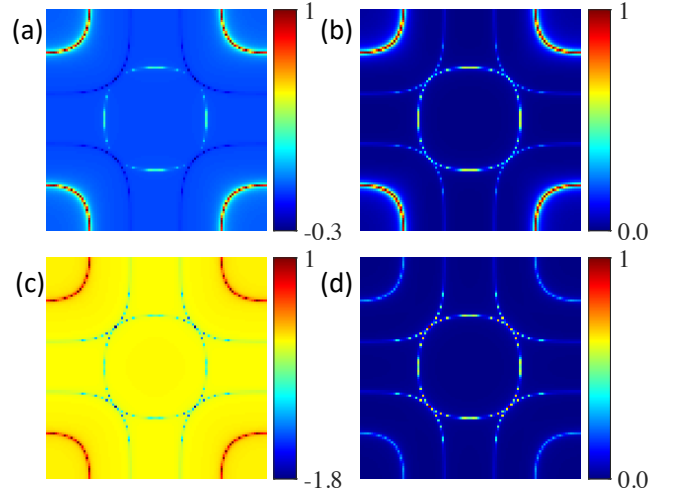


FIG. 7. The pairing gaps with fixed $\mu = 0eV$. (a) and (b) marks the pairing gap in the full-coupling case with fixed parameters $g_1^f = 0.07$ and $g_2^f = 0.12$ while varying pair hopping $g_P = -0.02$ and 0.02 , respectively. (c) and (d) illustrates the pairing gap in the half-coupling case with fixed parameters $g_1^h = 0.18$ and $g_2^h = 0.18$ while varying pair hopping $g_P = -0.02$ and 0.02 , respectively.

V. THE ROLE OF PAIR HOPPING INTERACTION

In multiband superconductivity, a pertinent question arises regarding the role of the pair-hopping term. To address this, we investigate the pairing symmetry by incorporating the pair-hopping term in both full and half-coupling scenarios. The pair hopping term reads

$$H_P = -g_P \sum_{\eta; \mathbf{k}, \mathbf{k}'; s, s'} c_{\eta x^2 s}^\dagger(-\mathbf{k}) c_{\eta x^2 s'}^\dagger(\mathbf{k}) c_{\eta z^2 s'}(\mathbf{k}') \times c_{\eta z^2 s}(-\mathbf{k}') \quad (18)$$

where g_P is the pair hopping strength. In the band space, it can be rewritten as

$$H_P = - \sum_{\mathbf{k}, \mathbf{k}'} \sum_{\beta \beta'; s s'} g_P^{\beta,\beta'}(\mathbf{k}, \mathbf{k}') c_{\beta s}^\dagger(\mathbf{k}) c_{\beta s'}^\dagger(-\mathbf{k}) \times c_{\beta' s'}(-\mathbf{k}') c_{\beta' s}(\mathbf{k}') \quad (19)$$

with

$$g_P^{\beta,\beta'}(\mathbf{k}, \mathbf{k}') = g_P \sum_{\eta} U_{\eta x^2 \beta}^*(\mathbf{k}) U_{\eta z^2 \beta}^*(-\mathbf{k}) U_{\eta x^2 \beta'}(-\mathbf{k}') \times U_{\eta z^2 \beta'}(\mathbf{k}'). \quad (20)$$

Then we can obtain

$$g^{\beta,\beta'} = g_1^{\beta,\beta'}(\mathbf{k}, \mathbf{k}') + g_2^{\beta,\beta'}(\mathbf{k}, \mathbf{k}') + g_P^{\beta,\beta'}(\mathbf{k}, \mathbf{k}'). \quad (21)$$

Compared to Fig.4(b), the numerical results presented in Fig.7(a) in the full-coupling model indicate that a negative pair-hopping interaction g_P tends to drive the superconducting state toward an alternative s_{\pm} -wave state. In

this state, the pairing gap on the α Fermi surface shares the same sign as the gap on the β Fermi surface but has the opposite sign compared to the gap on the γ Fermi surface. In contrast, a positive g_P in the full-coupling case favors the $s\pm$ -wave pairing symmetry. The preference for $s++$ -wave symmetry by negative and $s\pm$ -wave symmetry by positive g_P can be attributed to the fact that the Fermi surface is primarily composed of $d_{3z^2-r^2}$ orbital weight, while both the α and β Fermi surfaces have significant contributions from the $d_{x^2-y^2}$ orbital. Fig. 7 (c) and (d) lead to the conclusion that in the half-coupling case the pair-hopping strength g_P plays a similar role as in the full-coupling case.

VI. DISCUSSIONS AND CONCLUSIONS

In summary, we have systematically investigated the superconducting pairing symmetry mediated by effective attractive interactions in the celebrated high-temperature superconductor material $\text{La}_3\text{Ni}_2\text{O}_7$ under pressure. We considered two models, namely the full-coupling case in which the $\text{Ni-}d_{x^2-y^2}$ orbital and $d_{3z^2-r^2}$ orbital are treated equally in the interlayer and intralayer interactions, and the half-coupling case where the interlayer and intralayer coupling only includes $d_{3z^2-r^2}$ and

$d_{x^2-y^2}$ orbital, respectively. By solving the linear gap equation numerically, we have found that in the both cases the interlayer coupling tends to trigger the $s\pm$ superconducting state with a sign change between β and α (γ) Fermi surfaces, while the intralayer coupling leads to a pure $s++$ -wave without sign change between Fermi surfaces. Hence our calculations have revealed the competitive effect between interlayer and intralayer coupling, and also uncover that the final pairing symmetry arise from the nature of electronic wave-functions near Fermi level of the material under pressure. In addition, we also have considered the pair hopping interaction between $d_{3z^2-r^2}$ and $d_{x^2-y^2}$ orbitals, and have demonstrated that the repulsive pair hopping favors the $s\pm$ pairing symmetry as expected due to the fact γ and α Fermi surface mainly is mainly contributed from the $d_{3z^2-r^2}$ and $d_{x^2-y^2}$, respectively.

VII. ACKNOWLEDGE

We thank Xianxin Wu for very helpful discussions. Xinloong Han is supported by National Natural Science Foundation of China (Grant No. 12404162). Yucong Yin and Boyang Liu are supported by the National Science Foundation of China (Grant No. NSFC-11874002).

* boyangleo@gmail.com

† hanxinloong@gmail.com

¹ J. G. Bednorz and K. A. Müller, *Zeitschrift für Physik B Condensed Matter* **64**, 189 (1986).

² P. W. Anderson, *science* **235**, 1196 (1987).

³ P. A. Lee, N. Nagaosa, and X.-G. Wen, *Reviews of modern physics* **78**, 17 (2006).

⁴ B. Keimer, S. A. Kivelson, M. R. Norman, S. Uchida, and J. Zaanen, *Nature* **518**, 179 (2015).

⁵ Y. Kamihara, T. Watanabe, M. Hirano, and H. Hosono, *Journal of the American Chemical Society* **130**, 3296 (2008).

⁶ M. Daghofer, A. Moreo, J. A. Riera, E. Arrigoni, D. J. Scalapino, and E. Dagotto, *Phys. Rev. Lett.* **101**, 237004 (2008).

⁷ S. Raghu, X.-L. Qi, C.-X. Liu, D. J. Scalapino, and S.-C. Zhang, *Phys. Rev. B* **77**, 220503 (2008).

⁸ A. V. Chubukov, D. V. Efremov, and I. Eremin, *Phys. Rev. B* **78**, 134512 (2008).

⁹ H. Eschrig and K. Koepernik, *Phys. Rev. B* **80**, 104503 (2009).

¹⁰ G. R. Stewart, *Rev. Mod. Phys.* **83**, 1589 (2011).

¹¹ D. Li, K. Lee, B. Y. Wang, M. Osada, S. Crossley, H. R. Lee, Y. Cui, Y. Hikita, and H. Y. Hwang, *Nature* **572**, 624 (2019).

¹² E. Been, W.-S. Lee, H. Y. Hwang, Y. Cui, J. Zaanen, T. Devereaux, B. Moritz, and C. Jia, *Phys. Rev. X* **11**, 011050 (2021).

¹³ K.-W. Lee and W. E. Pickett, *Phys. Rev. B* **70**, 165109 (2004).

¹⁴ M. Hepting, D. Li, C. Jia, H. Lu, E. Paris, Y. Tseng, X. Feng, M. Osada, E. Been, Y. Hikita, *et al.*, *Nature materials* **19**, 381 (2020).

¹⁵ A. S. Botana and M. R. Norman, *Phys. Rev. X* **10**, 011024 (2020).

¹⁶ X. Wu, D. Di Sante, T. Schwemmer, W. Hanke, H. Y. Hwang, S. Raghu, and R. Thomale, *Phys. Rev. B* **101**, 060504 (2020).

¹⁷ M. Jiang, M. Berciu, and G. A. Sawatzky, *Phys. Rev. Lett.* **124**, 207004 (2020).

¹⁸ H. Sun, M. Huo, X. Hu, J. Li, Z. Liu, Y. Han, L. Tang, Z. Mao, P. Yang, B. Wang, *et al.*, *Nature* **621**, 493 (2023).

¹⁹ J. Hou, P. Yang, Z. Liu, J. Li, P. Shan, L. Ma, G. Wang, N. Wang, H. Guo, J. Sun, *et al.*, *Chinese Physics Letters* **40**, 117302 (2023).

²⁰ Y. Zhang, D. Su, Y. Huang, Z. Shan, H. Sun, M. Huo, K. Ye, J. Zhang, Z. Yang, Y. Xu, *et al.*, *Nature Physics* , 1 (2024).

²¹ G. Wang, N. N. Wang, X. L. Shen, J. Hou, L. Ma, L. F. Shi, Z. A. Ren, Y. D. Gu, H. M. Ma, P. T. Yang, Z. Y. Liu, H. Z. Guo, J. P. Sun, G. M. Zhang, S. Calder, J.-Q. Yan, B. S. Wang, Y. Uwatoko, and J.-G. Cheng, *Phys. Rev. X* **14**, 011040 (2024).

²² Z. Luo, X. Hu, M. Wang, W. Wú, and D.-X. Yao, *Physical review letters* **131**, 126001 (2023).

²³ F. Lechermann, J. Gondolf, S. Bötzel, and I. M. Eremin, *Physical Review B* **108**, L201121 (2023).

²⁴ Y. Gu, C. Le, Z. Yang, X. Wu, and J. Hu, *arXiv preprint arXiv:2306.07275* (2023), <https://doi.org/10.48550/arXiv.2306.07275>.

- ²⁵ Q.-G. Yang, D. Wang, and Q.-H. Wang, *Physical Review B* **108**, L140505 (2023).
- ²⁶ V. Christiansson, F. Petocchi, and P. Werner, *Physical Review Letters* **131**, 206501 (2023).
- ²⁷ H. Sakakibara, N. Kitamine, M. Ochi, and K. Kuroki, *Physical Review Letters* **132**, 106002 (2024).
- ²⁸ D. Shilenko and I. Leonov, *Physical Review B* **108**, 125105 (2023).
- ²⁹ Y. Shen, M. Qin, and G.-M. Zhang, *Chinese Physics Letters* **40**, 127401 (2023).
- ³⁰ Z. Liu, M. Huo, J. Li, Q. Li, Y. Liu, Y. Dai, X. Zhou, J. Hao, Y. Lu, M. Wang, *et al.*, *Nature Communications* **15**, 7570 (2024).
- ³¹ W. Wú, Z. Luo, D.-X. Yao, and M. Wang, *Science China Physics, Mechanics & Astronomy* **67**, 117402 (2024).
- ³² X. Chen, P. Jiang, J. Li, Z. Zhong, and Y. Lu, *Phys. Rev. B* **111**, 014515 (2025).
- ³³ Y. Cao and Y.-f. Yang, *Physical Review B* **109**, L081105 (2024).
- ³⁴ Y.-B. Liu, J.-W. Mei, F. Ye, W.-Q. Chen, and F. Yang, *Physical Review Letters* **131**, 236002 (2023).
- ³⁵ Y. Zhang, L.-F. Lin, A. Moreo, and E. Dagotto, *Phys. Rev. B* **108**, L180510 (2023).
- ³⁶ C. Lu, Z. Pan, F. Yang, and C. Wu, *Phys. Rev. Lett.* **132**, 146002 (2024).
- ³⁷ Y. Zhang, L.-F. Lin, A. Moreo, T. A. Maier, and E. Dagotto, *Nature Communications* **15**, 2470 (2024).
- ³⁸ H. Oh and Y.-H. Zhang, *Phys. Rev. B* **108**, 174511 (2023).
- ³⁹ Z. Liao, L. Chen, G. Duan, Y. Wang, C. Liu, R. Yu, and Q. Si, *Phys. Rev. B* **108**, 214522 (2023).
- ⁴⁰ X.-Z. Qu, D.-W. Qu, J. Chen, C. Wu, F. Yang, W. Li, and G. Su, *Phys. Rev. Lett.* **132**, 036502 (2024).
- ⁴¹ Y.-f. Yang, G.-M. Zhang, and F.-C. Zhang, *Phys. Rev. B* **108**, L201108 (2023).
- ⁴² K. Jiang, Z. Wang, and F.-C. Zhang, *Chinese Physics Letters* **41**, 017402 (2024).
- ⁴³ Y. Zhang, L.-F. Lin, A. Moreo, T. A. Maier, and E. Dagotto, *Phys. Rev. B* **108**, 165141 (2023).
- ⁴⁴ J. Huang, Z. D. Wang, and T. Zhou, *Phys. Rev. B* **108**, 174501 (2023).
- ⁴⁵ Y.-H. Tian, Y. Chen, J.-M. Wang, R.-Q. He, and Z.-Y. Lu, *Phys. Rev. B* **109**, 165154 (2024).
- ⁴⁶ Q. Qin and Y.-f. Yang, *Phys. Rev. B* **108**, L140504 (2023).
- ⁴⁷ G. Heier, K. Park, and S. Y. Savrasov, *Physical Review B* **109**, 104508 (2024).
- ⁴⁸ R. Khasanov, T. J. Hicken, D. J. Gawryluk, L. P. Sorel, S. Bötzel, F. Lechermann, I. M. Eremin, H. Luetkens, and Z. Guguchia, *arXiv preprint arXiv:2402.10485* (2024), <https://doi.org/10.48550/arXiv.2402.10485>.
- ⁴⁹ Y. Meng, Y. Yang, H. Sun, S. Zhang, J. Luo, L. Chen, X. Ma, M. Wang, F. Hong, X. Wang, *et al.*, *Nature Communications* **15**, 10408 (2024).
- ⁵⁰ J. Yang, H. Sun, X. Hu, Y. Xie, T. Miao, H. Luo, H. Chen, B. Liang, W. Zhu, G. Qu, *et al.*, *Nature Communications* **15**, 4373 (2024).
- ⁵¹ X.-W. Yi, Y. Meng, J.-W. Li, Z.-W. Liao, W. Li, J.-Y. You, B. Gu, and G. Su, *Physical Review B* **110**, L140508 (2024).
- ⁵² Z. Liu, M. Huo, J. Li, Q. Li, Y. Liu, Y. Dai, X. Zhou, J. Hao, Y. Lu, M. Wang, and H.-H. Wen, *Nature Communications* **15**, 7570.
- ⁵³ Z. Liu, H. Sun, M. Huo, X. Ma, Y. Ji, E. Yi, L. Li, H. Liu, J. Yu, Z. Zhang, *et al.*, *Science China Physics, Mechanics & Astronomy* **66**, 217411 (2023).
- ⁵⁴ B. Geisler, J. J. Hamlin, G. R. Stewart, R. G. Hennig, and P. Hirschfeld, *npj Quantum Materials* **9**, 38 (2024).
- ⁵⁵ E. Talantsev and V. Chistyakov, *Letters on Materials* **14**, 262 (2024).
- ⁵⁶ Y. Li, Y. Cao, L. Liu, P. Peng, H. Lin, C. Pei, M. Zhang, H. Wu, X. Du, W. Zhao, *et al.*, *arXiv preprint arXiv:2403.05012* (2024), <https://doi.org/10.48550/arXiv.2403.05012>.
- ⁵⁷ J.-Y. You, Z. Zhu, M. Del Ben, W. Chen, and Z. Li, *npj Computational Materials* **11**, 3 (2025).
- ⁵⁸ Z. Ouyang, M. Gao, and Z.-Y. Lu, *npj Quantum Materials* **9**, 80 (2024).
- ⁵⁹ J. Zhan, Y. Gu, X. Wu, and J. Hu, *arXiv preprint arXiv:2404.03638* (2024), <https://doi.org/10.48550/arXiv.2404.03638>.
- ⁶⁰ Y.-Z. Chou, F. Wu, J. D. Sau, and S. Das Sarma, *Physical review letters* **127**, 187001 (2021).